Nuclear Materials and Energy 28 (2021) 101045

Contents lists available at ScienceDirect

Nuclear Materials and Energy

journal homepage: www.elsevier.com/locate/nme

Cross machine investigation of magnetic tokamak dust; structural and magnetic analysis

M. De Angeli [a,*], P. Tolias [b], C. Conti [c], D. Ripamonti [d], F. Ghezzi [a], C. Arnas [e], J. Irby [f], M. Jerab [g], B. LaBombard [h], S. Lecci [i], G. Maddaluno [i]

[a] Institute for Plasma Science and Technology, CNR, via Cozzi 53, 20125 Milano, Italy
[b] Space and Plasma Physics - KTH Royal Institute of Technology, Teknikringen 31, 10044 Stockholm, Sweden
[c] Institute of Heritage Science, CNR, via Cozzi 53, 20125 Milano, Italy
[d] Institute of Condensed Matter Chemistry and Energy Technologies, CNR, via Cozzi 53, Milano, Italy
[e] CNRS, Aix-Marseille Université, Laboratoire PIIM, campus St Jérôme, 13397 Marseille, France
[f] M.I.T. Plasma Science and Fusion Center, 190 Albany Street, Cambridge, MA 02139, USA
[g] Institute of Plasma Physics of the CAS, Za Slovankou 3, 182 00 Prague 8, Czech Republic
[h] M.I.T. Plasma Science and Fusion Center, 175 Albany Street, Cambridge, MA 02139, USA
[i] ENEA, Fusion and Nuclear Safety Department, C. R. Frascati, Roma, Italy

ARTICLE INFO

Keywords:
Magnetic dust
Paramagnetic dust
Dust in tokamaks
FTU dust
Magnetic force
X-ray diffraction

ABSTRACT

Magnetic dust collected from multiple fusion devices (FTU, Alcator C-Mod, COMPASS) that feature different plasma-facing components (PFCs) and toroidal magnetic fields has been analyzed by means of the X-ray diffraction technique aiming to investigate the nature and origin of dust magnetism. Analysis led to the conclusion that the main mechanism of ferromagnetic dust formation is the change of iron crystalline phase from austenitic to ferritic during the re-solidification of stainless steel droplets. Analysis also revealed differences in the collected dust structure and an unexpectedly high amount of stainless steel based dust in its native austenitic phase. Theoretical estimates showed that the magnetic moment force can also mobilize strongly paramagnetic adhered dust prior to the establishment of proper tokamak discharges. The post-mortem analysis of dust collected during pure magnetic discharges in FTU confirmed these estimates.

1. Introduction

Tokamak dust, as a safety and operational issue, has been studied for more than two decades [1–4]. On the other hand, magnetic dust in tokamaks constitutes a recent line of investigation. Even though magnetic materials are not employed in tokamaks owing to the strong magnetic fields, the presence of magnetic dust has been documented in various fusion devices with different PFC composition [5–7]. In particular, the first collection of magnetic tokamak dust was reported in TEXTOR (~15wt% of dust collected) [5], followed by Globus-M (~10wt%) [6] & FTU (~30wt%) [7]. The main peculiarity of magnetic dust compared to non-magnetic dust lies in the former's propensity to mobilize, under the action of the strong applied magnetic fields, even before the plasma discharges are established. In this manner, magnetic dust traversing the vessel during the breakdown and the ramp-up startup phases can interfere with the realization of proper plasma discharges [8]. It is, thus, important to investigate the characteristics of magnetic tokamak dust, understand the origin of magnetic properties and elucidate the pre-plasma mobilization mechanism.

A comparative study of the morphological and elemental characteristics of magnetic dust collected from different tokamaks (Alcator C-Mod, COMPASS, DIII-D, FTU) was recently performed by the authors [9]. In this paper, the structural characteristics of the same magnetic dust collected from the FTU, Alcator C-Mod and COMPASS tokamaks are analyzed by means of the X-ray diffraction (XRD) technique. Note that the dust collected from DIII-D was too minuscule to allow for XRD analysis. The XRD results are employed to draw conclusions about the dominant form of magnetism as well as the nature of the phase transition that generates ferromagnetic dust. In addition, the magnetic force acting on adhered magnetic dust is evaluated. Finally, a detailed analysis of dust collected during pure magnetic discharges in FTU is presented.

As previously done in the literature [5–9], the term magnetic dust is employed herein in order to describe the entire dust fraction that can be collected by the use of a permanent magnet, regardless of the magnetism form (ferromagnetism, paramagnetism) and the actual magnetic permeability values of the individual dust particulates.

* Corresponding author.
E-mail address: marco.deangeli@istp.cnr.it (M. De Angeli).

https://doi.org/10.1016/j.nme.2021.101045
Received 17 May 2021; Received in revised form 13 July 2021; Accepted 18 July 2021
Available online 21 July 2021

Table 1
Vessel material composition at the time of the dust collection together with the maximum strength of the toroidal magnetic field. TZM is a molybdenum dominated alloy (Ti 0.5wt%, Zr 0.1wt%, Mo balance); SS stands for stainless steel; Inconel is a Ni based super-alloy.

Tokamak device	Wall material	Machine configuration	Limiter or divertor material	Maximum toroidal magnetic field
FTU	SS 304LN	Limiter	TZM	8.0 T
Alcator C-Mod	Mo	Divertor	Mo	8.0 T
COMPASS	Inconel 625	Divertor	Graphite	2.1 T

2. General characteristics

The magnetic dust batches under investigation have been collected from devices that feature different plasma-facing materials and maximum toroidal magnetic field strengths, as shown in Table 1. It is worth noting that the first wall composition in FTU (stainless steel - SS) and COMPASS (Inconel) is such that generation of magnetic dust can be directly seeded, while the same does not apply for the all-molybdenum Alcator C-Mod. However, additional sources of magnetic dust are SS-based diagnostics, antennas and structural materials that are present in all tokamaks. In terms of shape, the collected magnetic dust can be classified into flakes or debris, splashes and spheroids with the latter further separated into two sub-classes depending on the presence of a clear dendrite-like surface texture [9]. In terms of composition, the collected magnetic dust is either close to nickel-based alloys or austenitic SS (Fe, Cr, Ni) [9].

The magnetic dust batches considered in this work contain a sufficient amount of particulates so that their structural analysis by means of the XRD diagnostic is possible. The **FTU batch** has a 12.6 g weight, features particulates with $< 210\,\mu m$ size and was collected from the floor in 2017. The **COMPASS batch** of 0.042 g weight was collected from the divertor at the Langmuir probe feed-through position in 2014/15. The **Alcator C-Mod batch** of 0.074 g weight mainly consists of flakes or debris and was collected from the floor, the upper areas of the lower outer divertor, the horizontal areas and beneath the "FG" sector of the outer divertor in 2007. Examples of magnetic dust from the 4 morphological classes are shown in Fig. 1.

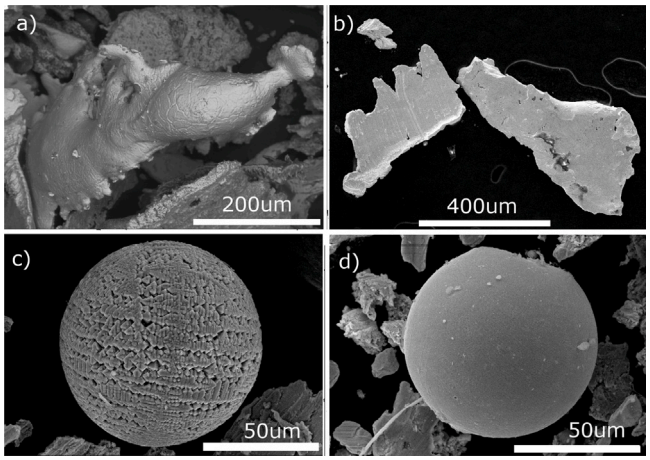

Fig. 1. Examples of electron microscope images of SS-based magnetic dust, collected from the three tokamaks investigated and classified on a morphological basis: (a) splashes from FTU; (b) flakes from Alcator C-Mod; (c) spheroids with dendrite-like surface texture from COMPASS; (d) spheroids without any evidence of dendrite-like surface texture from COMPASS.

3. X-ray Diffraction (XRD) analysis

Aiming to investigate the crystalline structure of the magnetic dust, the dust batches collected from different devices have been analyzed in a Bragg–Brentano geometry with a Panalytical X'Pert PRO X-ray powder diffractometer that is equipped with a Cu–K radiation source ($\lambda \sim 1.54$ Å) and a X'Celerator solid state detector PW3015/20 nickel filtered. The accelerating voltage and electric current at the Cu anode were set to 40 kV and 40 mA, respectively. The diffraction data were collected with a stepsize of 0.01° and a scan-step time ranging within 20.95–123.04 s.

3.1. Analysis of the XRD spectra

FTU dust. The XRD spectra of the magnetic dust batch versus the non-magnetic dust batch collected in FTU are illustrated in Fig. 2. The *non-magnetic dust batch spectrum* contains peaks due to the presence of iron in the face-centered cubic (fcc) crystalline structure, *i.e.* the non-magnetic allotropic form also known as austenitic form or Fe-γ phase, and peaks owing to the presence of some Ni alloys, Mo and Al_2O_3. Additional quartz peaks at 22–28° have not been shown for convenience. The Ni-based alloys stem from Inconel^{TM} 625 PFCs, while Mo stems from the limiter tiles. On the other hand, the *magnetic dust batch spectrum* contains some obvious peaks due to the presence of iron in the body-centered cubic (bcc) crystalline structure, *i.e.* the magnetic ferrite form, either in the Fe-α or Fe-δ phase. The Fe-γ peaks are visible at a relatively lower intensity, suggesting a higher proportion of the bcc

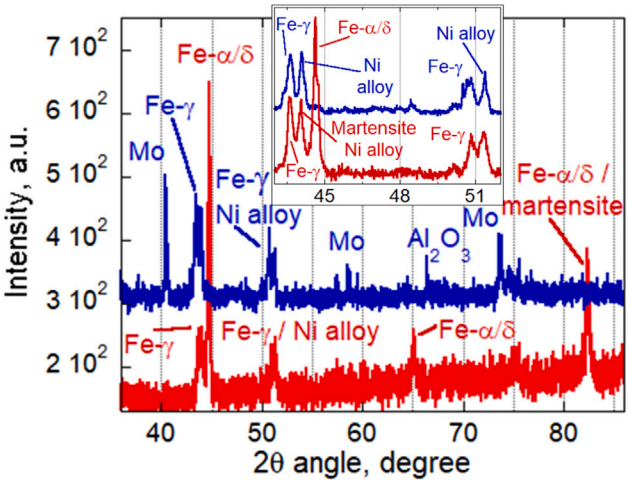

Fig. 2. XRD spectra of the magnetic (red line) and non-magnetic (blue line) dust batches collected from FTU. The insert shows the XRD spectra, at higher resolution, within 42–53°, *i.e.* in the range where typical SS peaks are located. The non-magnetic dust spectrum has been magnified by a factor 1.5 to improve visibility. (For interpretation of the references to color in this figure legend, the reader is referred to the web version of this article.)

phase compared to the fcc phase. An additional peak is present between the austenitic and ferritic peaks, at about 44.00°, that is likely due to, either, iron in the form of martensite (magnetic) or Ni compounds (see insert). A similar peak was detected in the non-magnetic dust batch, but it is unlikely that it is due to the presence of martensite, since the other martensite-related peak at 82.10° was not visible.

COMPASS dust. The XRD spectra of the magnetic dust batch are shown in Fig. 3, together with the FTU magnetic dust XRD spectra in order to facilitate comparison. This spectrum also contains a ferritic peak that exceeds the austenitic peak. However, the ratio between the ferritic and austenitic peak in the COMPASS spectrum is lower than that in the FTU spectrum. In addition, no appreciable peaks have been detected in this batch that could be attributed to the presence of Ni alloys or of martensite. The XRD spectra of the non-magnetic dust batch are also shown, but they are featureless in the 2θ angle range from 30° to 80°. Note that some peaks, that are attributed to quartz and C allotropes, are present between 25° and 30° (not shown in Fig. 3). The

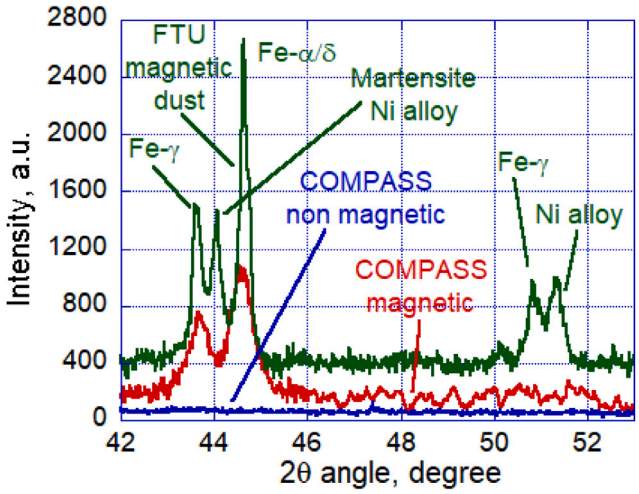

Fig. 3. XRD spectra of magnetic dust batches from FTU (green line) and from COMPASS (red line), together with those of the non-magnetic dust batch from COMPASS (blue line). Apart from some secondary SS peaks in the magnetic batch and quartz & carbon peaks in the non-magnetic batch, no additional peaks are present outside the narrow angular range depicted. The FTU magnetic dust spectrum has been magnified by a factor 4 to improve visibility. (For interpretation of the references to color in this figure legend, the reader is referred to the web version of this article.)

strong presence of carbon material in the non-magnetic dust batch was also confirmed by energy-dispersive X-ray (EDX) investigations.

Alcator C-Mod dust. The XRD spectra of the magnetic dust batch are almost identical to those of untreated AISI 316 grade dust, as revealed in Fig. 4a. A subclass of the magnetic dust batch has been further separated by means of a weaker permanent magnet in order to verify the presence of a non-negligible quantity of ferrite iron, as shown in Fig. 4b. The new XRD spectrum shows an increase of the ferritic peak compared to the austenitic peak, thus verifying the presence of non-negligible SS dust amount in ferrite form. The XRD results are consistent with the morphological analysis of the Alcator C-Mod magnetic dust, which revealed that the large majority of particulates is composed of SS-based flakes and debris [9]. Such dust grains are unlikely to have been subject to melting and re-solidification; the most common mechanism responsible for crystalline phase change from austenitic to ferritic in fusion devices. Finally, it is instructive to compare the spectrum of the magnetic dust batch with that of the non-magnetic batch, as done in Fig. 5. The spectrum of the non-magnetic batch does not contain any austenitic peak leading to the conclusion that all the SS-based dust particles, ferromagnetic and paramagnetic, have been classified as "magnetic dust".

3.2. Discussion of the XRD spectra

In tokamaks, the iron-based dust is generated by the interaction between the plasma and the SS-based structural or plasma-facing components, such as diagnostics and antennas. The amount of magnetic dust is particularly high in FTU ($\sim 30\,wt\%$) due to its AISI304 steel first wall composition, see Table 1. The austenitic peak present in the XRD spectra indicates the presence of SS dust in an untreated form, *i.e.* flakes and debris, that do not show any evidence of melting under plasma interaction. On the other hand, the ferritic peak present in the XRD spectra indicates the realization of a phase transition from the austenitic to the ferritic form that is caused by the interaction between the SS material and the incident plasma [7]. In addition, the FTU XRD spectra reveal a peak consistent with the presence of martensite. Martensite, whose crystal structure is body-centered tetragonal (bct), is a supersaturated solid solution of carbon in iron which results from the diffusion-less transformation that occurs when austenite is rapidly cooled down.

The main mechanisms leading to the phase transition from the austenitic to the ferritic (or even the martensitic) form in fusion devices are: **(a)** the generation of ferromagnetic induced structures, *i.e.* from Fe-γ to Fe-α, during the re-solidification of SS droplets in the presence of a strong magnetic field [10,11], **(b)** the Fe-δ phase stabilization due to the temperature quench of SS droplets [12,13], **(c)** the depletion of γ-stabilizing elements such as Mn or Ni in SS droplets [14,15] due to sputtering or evaporation, **(d)** magnetomechanical effects induced by SS machining [16,17].

From the XRD spectra of the magnetic dust batches collected from different devices, it is evident that the dominant mechanism responsible for the generation of magnetic dust can differ between devices. The **FTU spectra** suggest (a) and (b) as the main mechanisms of magnetic dust formation. The presence of martensite constitutes evidence for the likely realization of mechanism (b), since it can be originated when rapid cooling is involved. It should be noted that, while dust heating can be rapid in fusion devices due to the continuous absorption of plasma fluxes, dust cooling is generally slower being controlled by vaporization, electron emission and thermal radiation [18,19]. Most probably, the sudden temperature quench, necessary for mechanism (b), is realized by conduction and occurs once molten dust splashes on the vessel, FTU being a cryogenic device. The **COMPASS spectra** suggest that (a) is the dominant mechanism of magnetic dust generation, since they are similar to the FTU spectra, with the exception of the martensite and Ni alloy peaks. The **Alcator C-Mod spectra** are very similar to those of standard SS powder, which indicates that the main components of the batch are dust particulates (flakes, debris) in their native austenitic form. Even though a non-negligible amount of ferritic dust is present, most probably produced by mechanism (a), most of the magnetic dust in this batch referred to paramagnetic dust. Finally, the remaining mechanisms (c), (d) cannot be excluded and are probably still active in all devices, albeit not dominant. For example, chips generated by in-vessel works have been collected in Ref. [9].

XRD analysis led to the documentation of some conclusive evidence of different operative mechanisms that are capable of generating magnetic tokamak dust. It should be mentioned that the magnetic dust batches, considered in this investigation, may not be totally representative of the dust inventory of the respective devices. Nevertheless, independent of the actual origin of magnetization, the ability of magnetic dust to mobilize under the influence of strong external magnetic fields is an important issue for tokamak operations.

4. Magnetic force acting on paramagnetic grains

It has been demonstrated that strong tokamak magnetic fields are able to mobilize adhered ferromagnetic dust [8]. The abundance of paramagnetic SS dust that was revealed by the analysis of the XRD spectra of the Alcator C-Mod magnetic dust batch raises the question of whether these strong tokamak magnetic fields are also able to mobilize adhered paramagnetic dust of high magnetic susceptibility. In order to address this question, we shall assume perfectly spherical homogeneous dust.

The volumetric magnetic moment force that is exerted on a uniformly magnetized sphere is generally given by [20]

$$\boldsymbol{f}_{\nabla B} = (\boldsymbol{M}\cdot\nabla)\boldsymbol{B}\,, \tag{1}$$

with $\boldsymbol{M}$ the magnetization, $\boldsymbol{B}$ the total external magnetic field. For *ferromagnetic spherical dust*, owing to the strong applied B-fields, the magnetization will be instantaneously aligned with the toroidal magnetic field and will acquire its field-independent saturation value, $\boldsymbol{M} = M_s(T_d)\hat{\boldsymbol{b}}$. The temperature dependence will be dictated by Bloch's law, *i.e.* $M_s(T_d) = M_{s0}\left[1 - C(T_d/T_c)^{3/2}\right]$ with M_{s0} the saturation magnetization at absolute zero, T_c the Curie temperature, C a ferromagnetic material constant [21]. In our case, we have $C \ll 1$, $T_c \gg T_d$ which leads to $M_s(T_d) \simeq M_{s0}$ [8]. Substituting for the toroidal field $\boldsymbol{B} = (B_{t0}R_0/R)\hat{\boldsymbol{e}}_\phi$

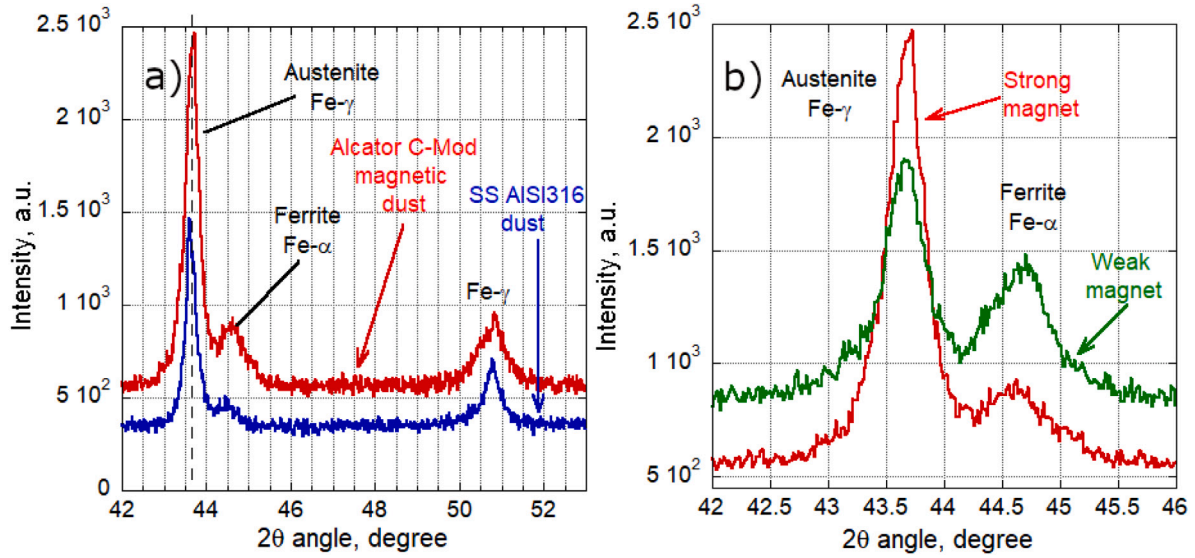

Fig. 4. XRD spectra of dust collected from Alcator C-Mod. (a) Spectra of magnetic dust batch (red line) compared to those of untreated SS AISI 316 grade dust (standard reference material 166c - Stainless Steel AISI 316). Apart from some secondary SS peaks, no additional peaks are present outside the narrow angular range depicted. (b) Spectra of the magnetic dust batch (red line) compared to those of a magnetic dust batch subclass collected by means of a weaker magnet (green line) around the locations of the main austenitic and ferritic peaks. (For interpretation of the references to color in this figure legend, the reader is referred to the web version of this article.)

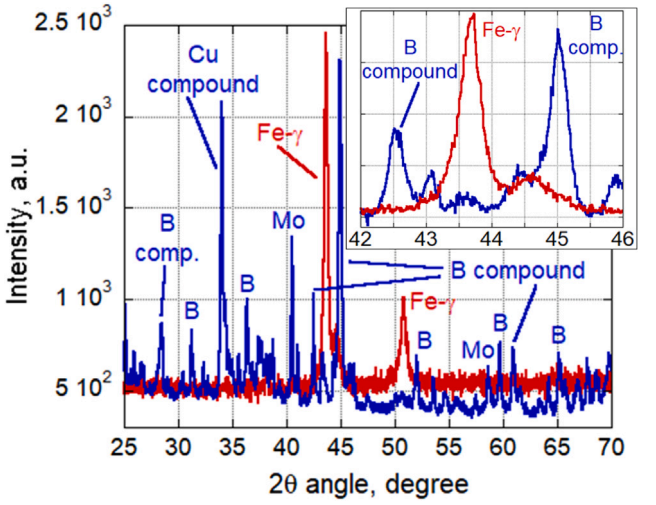

Fig. 5. XRD spectra of magnetic (red line) and non-magnetic (blue line) dust batches collected from Alcator C-Mod. The designation "B compound" stands for iron, tungsten or molybdenum borides. The insert shows the XRD spectra, at higher resolution, within 42–46°, where the typical austenitic peak is located. The magnetic dust spectrum has been magnified by a factor 1.76 to improve visibility. (For interpretation of the references to color in this figure legend, the reader is referred to the web version of this article.)

with B_{t0} the field strength at the torus axis, R_0 the major radius and R the radial dust position, one ends up with [8]

$$\boldsymbol{f}^{\mathrm{fer}}_{\nabla B} = -M_{s0}\frac{B_{t0}R_0}{R^2}\hat{\boldsymbol{e}}_R\,. \tag{2}$$

For *paramagnetic spherical dust*, we have $\boldsymbol{M} = \chi_v \boldsymbol{H}$ inside the grain with χ_v the volume magnetic susceptibility and $\boldsymbol{B} = \mu_0 \boldsymbol{H}$ in the vacuum ambient with μ_0 the permeability of free space. Combining the above with the magnetostatic relation $(\boldsymbol{B}\cdot\nabla)\boldsymbol{B} = \nabla B^2/2$, leads to a force density that reads as $(\chi_v/2\mu_0)\nabla B^2$ [22,23]. Substituting for the toroidal field $\boldsymbol{B} = (B_{t0}R_0/R)\hat{\boldsymbol{e}}_\phi$, one ends up with

$$\boldsymbol{f}^{\mathrm{par}}_{\nabla B} = -\frac{\chi_v}{\mu_0}\frac{B_{t0}^2R_0^2}{R^3}\hat{\boldsymbol{e}}_R\,. \tag{3}$$

Thus, the magnetic moment force for both ferromagnetic and paramagnetic dust is always directed towards the high-field side. Using $R \simeq R_0$ for an estimate, we obtain

$$\frac{f^{\mathrm{par}}_{\nabla B}}{f^{\mathrm{fer}}_{\nabla B}} \simeq \frac{\chi_v B_{t0}}{\mu_0 M_{s0}}\,. \tag{4}$$

For the SS values of $\chi_v = 4\times10^{-3}$, $M_{s0} = 1735\,\mathrm{kA/m}$ and with $B_{t0} = 5\,\mathrm{T}$, this leads to $f^{\mathrm{par}}_{\nabla B} \sim 0.01 f^{\mathrm{fer}}_{\nabla B}$. For the SS mass density of $\rho_m \simeq 8\,\mathrm{g/cm^3}$, we also obtain $f^{\mathrm{par}}_{\nabla B} \sim 2\rho_m g$. Thus, the magnetic dipole force on paramagnetic SS dust is a hundred times smaller than the magnetic dipole force on ferromagnetic SS dust, but it still exceeds the gravitational force by a factor of two.

We can now compare with the adhesive force resisting mobilization, given by the van der Waals formula [24,25]

$$F_{\mathrm{vdw}} = \frac{A}{6z_0^2}r_d\,, \tag{5}$$

where r_d is the dust radius, $z_0 \simeq 0.4$ nm is the distance of closest approach and A is the Hamaker constant. Systematic non-retarded Lifshitz calculations have led to the values $A(\mathrm{Fe}) = 3.92\times10^{-19}\,\mathrm{J}$, $A(\mathrm{Cr}) = 3.71\times10^{-19}\,\mathrm{J}$, $A(\mathrm{Ni}) = 3.73\times10^{-19}\,\mathrm{J}$ [26,27]. Therefore, $A(\mathrm{SS}) = 3.8\times10^{-19}\,\mathrm{J}$ should be an accurate estimate. It emerges that the magnetic moment force overcomes the adhesive force for $r_d \gtrsim 0.8\,\mathrm{mm}$. It is important to point out that nanometer scale surface roughness would lead to non-zero remobilization probabilities even for $r_d \sim 100\,\mu\mathrm{m}$ [8,25]. In addition, micrometer scale surface roughness would decrease the adhesion up to two orders of magnitude [28], while prolonged plasma treatment at elevated temperatures would increase adhesion up to two orders of magnitude [29]. Even with roughness effects included, the predicted size of remobilizable paramagnetic SS dust is rather large compared to that of metallic dust encountered in the JET [30], ASDEX-Upgrade [31] and WEST [32] tokamaks, with FTU [33] and Alcator C-Mod [34] being notable exceptions.

Finally, it should be noted that tungsten is slightly paramagnetic $\chi_v \simeq 5.6\times10^{-6}$ and that beryllium is slightly diamagnetic $\chi_v \simeq -1.8\times10^{-6}$ [35]. Their magnetic susceptibilities are three orders of magnitude lower than the magnetic susceptibility of paramagnetic stainless steel. Thus, magnetic moment forces on tungsten and beryllium dust are always negligible with respect to gravitational and adhesive forces. Consequently, magnetic moment forces cannot mobilize adhered tungsten or beryllium tokamak dust.

Table 2
Summary of the morphology and composition of the five dust particles that were collected during two consecutive pure magnetic discharges in FTU. EDX stands for Energy Dispersive X-ray spectroscopy and SEM stands for Scanning Electron Microscopy.

Dust label	Shape	Length or diameter, l or d	Main material by EDX	SEM image
1	Splashed stripe	l=4.5 mm	SS	6
2	Droplet with tail	d = 160 μm l = 2.5 mm	SS	7
3	Spheroid	d = 60 μm	SS	8a
4	Flake	l = 70 μm	SS	8b
5	Flake	l = 300 μm	SS	8c

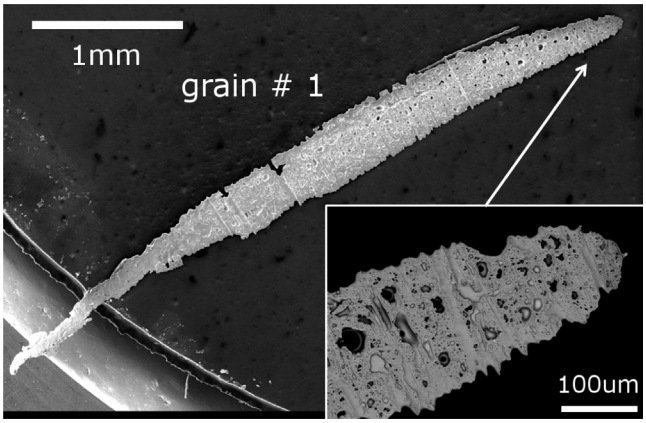

Fig. 6. SEM image of the entire elongated splashed stripe, labeled as grain #1, together with a zoom-in at its top side. The results of the EDX analysis of the area contained in the insert read as follows: Cr 19.1wt%, Fe 70.1wt%, Ni 10.3wt%, others 0.5wt%.

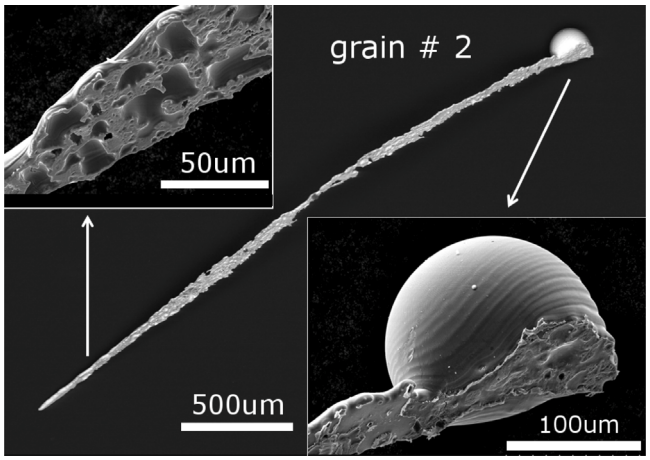

Fig. 7. SEM image of the re-solidified spheroidal droplet and its long tail, labeled as grain #2, together with the zoom-in both of the tail edge and of the droplet head. The results of the EDX analysis of the droplet head read as follows: C 3.5wt%, O 0.7wt%, Cr 17.3wt%, Fe 68.9wt%, Ni 9.6wt%.

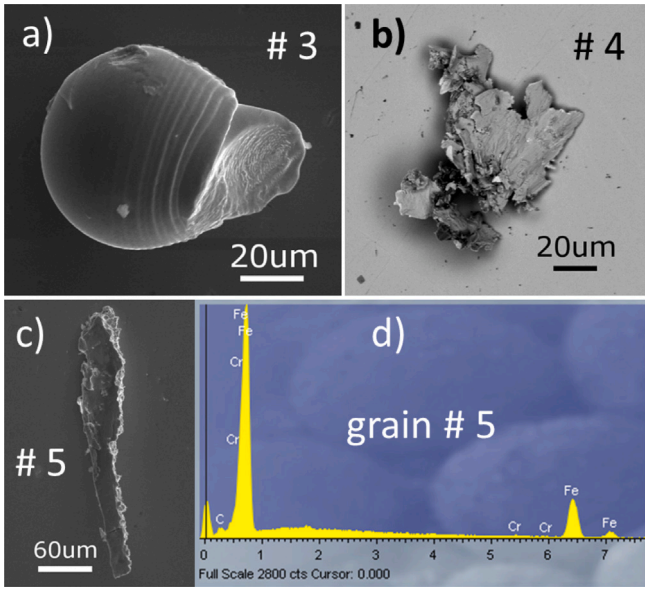

Fig. 8. (a) SEM image of the spheroidal particle, labeled as grain #3. (b) SEM image of the irregular flake, labeled as grain #4. (c) SEM image of the needle-like flake, labeled as grain #5. (d) The EDX spectrum of grain #5 revealing its SS composition.

5. Dust collection during pure magnetic discharges

In an effort to quantify the pre-plasma remobilization probability of magnetic dust, a dust collector plate was exposed in the FTU tokamak during pure magnetic field discharges. The collector comprised of a polished disk-shaped SS plate of 25 mm diameter and was exposed flush to the bottom of the vacuum vessel to two consecutive pure magnetic field discharges of a 5.4 T nominal toroidal magnetic field. The elevated rim prevented captured dust from rolling or sliding off the collector, while the polished surface reduced the probability that rolling or sliding dust would encounter a roughness ramp and then get detached [4]. Since the sticking velocity of micrometer-size metal dust does not drastically vary amongst vacuum compatible metals [18], an SS plate was chosen. Aerogel collectors [36] were not preferred due to the possibility of machine contamination with silica debris (given the large dust sizes) and technical difficulties.

Analysis, carried out by an electron microscope prior to and post exposure, revealed the presence of five large particles on the plate after the discharges. Their morphology and dimensions are reported in Table 2. The characteristic size of collected dust always exceeded 50 μm consistent with the prediction of a ~ 100 μm size threshold (smoothed by surface roughness) above which the magnetic moment force on ferromagnetic dust exceeds the adhesion force [8].

A morphological consideration together with the EDX analysis led to the conclusion that the magnetic dust particles #1, #2, #3 (see Figs. 6, 7, 8a) have been generated by the re-solidification of SS material. In fact, the surface waves that are clearly visible on the spherical dust #2, #3 are frozen capillary waves that constitute typical footprints of re-solidification of adhered dust [37,38]. On the other hand, there are no macro-morphological features in particles #4,#5 (Fig. 8b and c) that suggest re-solidification has taken place. Nevertheless, the EDX spectra prove their origin from SS-based PFCs, see Fig. 8d for particle #5.

Within the oversimplifying hypothesis that all the magnetic dust, which is mobilized all around the vacuum vessel by the toroidal magnetic field, will fall down on the vessel floor once the magnetic field is turned off, an estimation of the collected dust number during pure magnetic discharges is possible. By utilizing the average magnetic dust density value of $n_d \sim 10^{-2}\,cm^{-3}$ deduced for FTU [8] and the collecting volume of $V_{col} = 330\,cm^3$ (volume of the vacuum vessel column above the collector plate), the number of dust collected on the plate is estimated to be $n_d \times V_{col} \sim 3$ per discharge. The latter result is consistent with the 5 dust particles actually collected during two consecutive exposures to pure magnetic discharges, although the number of collected

dust particles is statistically insignificant. It should be pointed out that the starting hypothesis is only viable because the sticking velocity of $\gtrsim 100\,\mu m$ size dust is extremely small and, thus, the dust-PFC collisions lead to inelastic rebound and not to immobilization [4,18,39].

6. Summary and conclusions

The XRD spectra of magnetic dust batches collected from three tokamaks (Alcator C-Mod, COMPASS, FTU) are analyzed in order to investigate the dominant form of magnetism (ferromagnetism, strong paramgnetism) as well as the nature of the phase transition generating ferromagnetic dust from paramagnetic plasma-facing materials. Analysis revealed that the main mechanism leading to the formation of ferromagnetic dust is the change of crystalline phase from Fe-γ (austenite) to Fe-α/δ (ferrite) during the re-solidification of SS droplets. Nevertheless, a large amount of SS-based flakes and debris, that do not present any evidence of melting and re-solidification, was detected in all magnetic dust batches, especially in the Alcator-C-Mod batch where they constitute the dominant component.

The collection of such dust particles brought forth the issue of whether strongly paramagnetic dust could also be mobilized by the strong tokamak magnetic fields. Our estimates suggest that the magnetic moment force exerted on paramagnetic SS dust, although a hundred times smaller than that exerted on ferromagnetic dust, always exceeds gravity and overcomes adhesion for sub-millimeter range sizes. Thus, pre-plasma mobilization of the strongly paramagnetic SS dust is possible, but the same does not apply for the weakly magnetic tungsten or beryllium dust.

Moreover, post-mortem analysis of dust collected from FTU during pure magnetic discharges revealed the presence of both re-solidified SS droplets and SS-based flakes in a quantity consistent with earlier estimates of the density of the mobilized magnetic dust. The collection of SS-based flakes/debris demonstrates that large paramagnetic dust is indeed mobilized by the FTU toroidal magnetic field.

Finally, it is worth emphasizing that the magnetic field driven mobilization of ferromagnetic and strongly paramagnetic dust prior to plasma discharges [8] can be an important issue in the prospective of the possible extensive use of low activation steel [40] and austenitic stainless steel components [41] in future fusion reactors, *i.e.* ITER and DEMO, where plasma breakdown is critical. In fact, the latest ITER projections anticipate the generation of comparable amounts of stainless steel dust and tungsten dust by the end of the fusion power operation phase [42,43].

CRediT authorship contribution statement

M. De Angeli: Conceptualization, Investigation, Writing – original draft. **P. Tolias:** Formal analysis, Writing – review & editing. **C. Conti:** Investigation. **D. Ripamonti:** Investigation. **F. Ghezzi:** Validation. **C. Arnas:** Resources. **J. Irby:** Resources. **M. Jerab:** Resources. **B. LaBombard:** Resources. **S. Lecci:** Investigation. **G. Maddaluno:** Resources.

Declaration of competing interest

The authors declare that they have no known competing financial interests or personal relationships that could have appeared to influence the work reported in this paper.

Acknowledgments

The authors would like to thank Enrico Bassani for the acquisition of some XRD spectra. This work was co-funded by MEYS project LM2018117.

References

[1] J.P. Sharpe, D.A. Petti, H.-W. Bartels, Fusion Eng. Des. 63–64 (2002) 153.
[2] J. Roth, E. Tsitrone, A. Loarte, et al., J. Nucl. Mater. 390–391 (2009) 1.
[3] S.I. Krasheninnikov, R.D. Smirnov, D.L. Rudakov, Plasma Phys. Control. Fusion 53 (2011) 083001.
[4] P. Tolias, S. Ratynskaia, M. De Angeli, et al., Plasma Phys. Control. Fusion 58 (2016) 025009.
[5] J. Winter, Phys. Plasmas 7 (2000) 3862.
[6] A.N. Novokhatsky, A.E. Gorodetsky, V.K. Gusev, et al., Proc. 38th EPS Conf., Vol. 35G, 2011, Strasbourg, France, P5.066.
[7] M. De Angeli, L. Laguardia, G. Maddaluno, et al., Nucl. Fusion 55 (2015) 123005.
[8] M. De Angeli, E. Lazzaro, P. Tolias, et al., Nucl. Fusion 59 (2019) 106033.
[9] M. De Angeli, D. Ripamonti, F. Ghezzi, et al., Fusion Eng. Des. 166 (2021) 112315.
[10] J.H. Lee, T. Fukuda, T. Kakeshita, J. Phys. Conf. Ser. 156 (2009) 012013.
[11] J. Choi, T. Fukuda, T. Kakeshita, Alloys Compd. 577S (2013) S605.
[12] E. Franconi, J. Nucl. Mater. 179–181 (1991) 267.
[13] R. Andreani, ENEA Internal Report RT/FUS/86/7, 1986.
[14] V.N. Tsytovich, J. Winter, Phys.-Usp. 41 (1998) 815.
[15] K.H. Lo, C.H. Shek, J.K.L. Lai, Mater. Sci. Eng. R 65 (2009) 39.
[16] D.C. Jiles, J. Phys. D: Appl. Phys. 28 (1995) 1537.
[17] Y. Chen, B.K. Kriegermeier-Sutton, J.E. Snyder, et al., J. Magn. Magn. Mater. 236 (2001) 131.
[18] L. Vignitchouk, P. Tolias, S. Ratynskaia, Plasma Phys. Control. Fusion 56 (2014) 095005.
[19] S. Ratynskaia, P. Tolias, M. De Angeli, et al., Nucl. Fusion 58 (2018) 106023.
[20] W. Greiner, Classical Electrodynamics, Springer, New York, 1998.
[21] C. Kittel, Introduction to Solid State Physics, Wiley, New Jersey, 2005.
[22] R. Gerber, C.D. Wright, G. Asti, Applied Magnetism, Springer Science, Dordrecht, 1994.
[23] Q.A. Pankhurst, J. Connolly, S.K. Jones, J. Dobson, J. Phys. D: Appl. Phys. 36 (2003) R167.
[24] G. Riva, P. Tolias, S. Ratynskaia, et al., Nucl. Mater. Energy 12 (2017) 593.
[25] P. Tolias, G. Riva, M. De Angeli, et al., Nucl. Mater. Energy 15 (2018) 55.
[26] P. Tolias, Fusion Eng. Des. 133 (2018) 110.
[27] P. Tolias, Surf. Sci. 700 (2020) 121652.
[28] S. Peillon, A. Autricque, M. Redolfi, et al., J. Aerosol Sci. 137 (2019) 105431.
[29] P. Tolias, M. De Angeli, S. Ratynskaia, et al., Nucl. Mater. Energy 24 (2020) 100765.
[30] M. Rubel, A. Widdowson, J. Grzonka, et al., Fusion Eng. Des. 136 (2018) 579.
[31] M. Balden, N. Endstrasser, P.W. Humrickhouse, et al., Nucl. Fusion 54 (2014) 073010.
[32] S. Peillon, G. Dougniaux, M. Payet, et al., Nucl. Mater. Energy 24 (2020) 100781.
[33] M. De Angeli, G. Maddaluno, L. Laguardia, et al., J. Nucl. Mater. 463 (2015) 847.
[34] C. Arnas, J. Irby, S. Celli, et al., Nucl. Mater. Energy 11 (2017) 12.
[35] D.R. Lide, CRC Handbook, CRC Press, Boca Raton, 2004.
[36] S. Ratynskaia, H. Bergsåker, B. Emmoth, et al., Nucl. Fusion 49 (2009) 122001.
[37] S. Ratynskaia, P. Tolias, I. Bykov, et al., Nucl. Fusion 56 (2016) 066010.
[38] S. Ratynskaia, P. Tolias, M. De Angeli, et al., Nucl. Mater. Energy 12 (2017) 569.
[39] S. Ratynskaia, L. Vignitchouk, P. Tolias, et al., Nucl. Fusion 53 (2013) 123002.
[40] J. Roth, K. Sugiyama, V. Alimov, et al., J. Nucl. Mater. 454 (2014) 1.
[41] R.A. Pitts, B. Bazylev, J. Linke, et al., J. Nucl. Mater. 463 (2015) 748.
[42] G. De Temmerman, R.A. Pitts, Progress in the analysis of PWI issues for ITER and research needs, in: Joint Annual Meeting of WP-JET2 & WP-PFC, 10/11/2020.
[43] R.A. Pitts, Progress in the understanding of plasma-wall interactions in support of the ITER Research Plan, in: 47th EPS (virtual) Conference on Plasma Physics, 21/06/2021.